computation

MDPI

Article

Hybrid Nanofluid Flow over a Shrinking Rotating Disk: Response Surface Methodology

Rusya Iryanti Yahaya [1], Norihan Md Arifin [1,2,*], Ioan Pop [3], Fadzilah Md Ali [1,2] and Siti Suzilliana Putri Mohamed Isa [1,4]

[1] Institute for Mathematical Research, Universiti Putra Malaysia, Serdang 43400, Malaysia; rusyairyanti@gmail.com (R.I.Y.); fadzilahma@upm.edu.my (F.M.A.); ctsuzilliana@upm.edu.my (S.S.P.M.I.)
[2] Department of Mathematics and Statistics, Universiti Putra Malaysia, Serdang 43400, Malaysia
[3] Department of Mathematics, Babeş-Bolyai University, 400084 Cluj-Napoca, Romania; popm.ioan@yahoo.co.uk
[4] Centre of Foundation Studies for Agricultural Science, Universiti Putra Malaysia, Serdang 43400, Malaysia
* Correspondence: norihana@upm.edu.my

Abstract: For efficient heating and cooling applications, minimum wall shear stress and maximum heat transfer rate are desired. The current study optimized the local skin friction coefficient and Nusselt number in Al_2O_3-Cu/water hybrid nanofluid flow over a permeable shrinking rotating disk. First, the governing equations and boundary conditions are solved numerically using the bvp4c solver in MATLAB. Von Kármán's transformations are used to reduce the partial differential equations into solvable non-linear ordinary differential equations. The augmentation of the mass transfer parameter is found to reduce the local skin friction coefficient and Nusselt number. Higher values of these physical quantities of interest are observed in the injection case than in the suction case. Meanwhile, the increase in the magnitude of the shrinking parameter improved and reduced the local skin friction coefficient and Nusselt number, respectively. Then, response surface methodology (RSM) is conducted to understand the interactive impacts of the controlling parameters in optimizing the physical quantities of interest. With a desirability of 66%, the local skin friction coefficient and Nusselt number are optimized at 1.528780016 and 0.888353037 when the shrinking parameter (λ) and mass transfer parameter (S) are -0.8 and -0.6, respectively.

Keywords: disk; hybrid nanofluid; RSM; shrinking; suction/injection

Citation: Yahaya, R.I.; Arifin, N.M.; Pop, I.; Ali, F.M.; Isa, S.S.P.M. Hybrid Nanofluid Flow over a Shrinking Rotating Disk: Response Surface Methodology. *Computation* **2024**, *12*, 141. https://doi.org/10.3390/computation12070141

Academic Editors: Ali Cemal Benim, Abdulmajeed A. Mohamad, Sang-Ho Suh, Rachid Bennacer, Paweł Oclon and Jan Taler

Received: 28 June 2024
Revised: 6 July 2024
Accepted: 8 July 2024
Published: 10 July 2024

1. Introduction

Rotating machinery, gas turbine rotators, and thermal power generating systems are among the numerous practical applications of the classical rotating-disk flow [1]. The Navier–Stokes equations for rotating-disk flow were first presented by Von Kármán [2]. In this study, Von Kármán's transformations were introduced to reduce the partial differential equations into a system of ordinary differential equations. Later, these equations were employed in various rotating-disk flow problems. Ayano et al. [3] did a numerical computation on magnetohydrodynamics (MHD) nanofluid flow over a stretching rotating disk with Brownian motion, thermophoresis, and gyrotactic microorganisms. Von Kármán's transformations were employed in this study, and the increased stretching parameter was found to reduce the temperature profile. Meanwhile, the augmentation of the thermophoresis and Brownian motion enhanced and reduced the concentration profile. Then, the unsteady flow of nanofluid over a stretching rotating disk with variable viscosity, Brownian motion, and thermophoresis was analyzed by Sharma et al. [4]. It was found that the increased stretching rate promoted fluid flow in the radial direction and enhanced horizontal velocity. Puneeth et al. [5] then examined the unsteady flow over a permeable stretching rotating disk. It was observed that a high nanoparticle volume fraction improved and reduced the temperature and velocity profiles of the nanofluid.

Researchers have also examined the rotating-disk flow of hybrid nanofluids containing the dispersion of two different nanoparticles. Rashid et al. [6] analyzed the MHD hybrid nanofluid flow over a rotating disk with Brownian motion and thermophoresis. It was noted that the hybrid nanofluid possessed better thermal conductivity than the nanofluid. Moreover, the augmentation of the magnetic field reduced axial and tangential velocities while increasing the surface drag. Meanwhile, thermophoresis and nanoparticle volume fraction enhanced the heat transfer performance. Alkuhayli [7] extended this study with thermal radiation and heat source/sink. The enhancement of the thermal radiation and variable thermal conductivity parameters was found to have boosted the temperature profile and local Nusselt number. Further extension of this study was made by Kumar et al. [8], who considered the electromagnetohydrodynamic flow over a stretching rotating disk with an irregular heat source, Arrhenius energy, and non-linear radiation. The increment in the electric parameter was noted to reduce the skin friction coefficient and enhance the heat transfer rate. Meanwhile, Kulkarni [9] found that the heat transfer rate increased with the sphericity of the nanoparticles in hybrid nanofluid flow over a permeable rotating disk with mixed convection, magnetic field, and slip. Lone et al. [10] then analyzed the MHD flow of Al_2O_3-Cu/water hybrid nanofluid over a rotating disk with velocity slip, zero mass flux, and convective boundary conditions. Next, Khashi'ie et al. [11] conducted a stability analysis on multiple solutions obtained in MHD hybrid nanofluid flow over a permeable stretching/shrinking rotating disk with heat generation. The findings revealed that only the first and second solutions were stable and physically significant, while the third solution was unstable. In addition, only the suction parameter enhanced the heat transfer performance of the hybrid nanofluid. Vijay and Sharma [12] then studied the Soret and Dufour effects on MHD hybrid nanofluid flow over a permeable decelerating rotating disk. Later, Abu Bakar et al. [13] analyzed the unsteady flow of Al_2O_3-Cu/water hybrid nanofluid over an inclined, shrinking, rotating disk with thermal radiation and velocity slip. Similarly, only the first solution was found to be stable, while the second solution was unstable. The nanoparticle volume fraction, radiation, and shrinking parameters increased the heat transfer rate. Recently, the rotating-disk flow of ternary and tetra hybrid nanofluids, consisting of three and four different nanoparticles dispersed in a base fluid, was also analyzed by researchers (see Ali et al. [14], Singh et al. [15], and Patgiri and Paul [16]). In addition, researchers have also incorporated machine learning approaches to study fluid flow over a rotating disk (see Ali et al. [17] and Kumar et al. [18]).

Moreover, researchers have also included statistical analysis to improve theoretical investigations of fluid flow over a rotating disk. A sophisticated statistical tool called the response surface methodology (RSM) is commonly employed to analyze the effects and significance of various controlling parameters on specified responses. The optimal conditions at which to achieve the desired response can also be estimated using the RSM. Mehmood et al. [19] utilized the RSM to optimize the local skin friction coefficients and Nusselt number in MHD nanofluid flow past a stretched rotating disk with entropy generation and autocatalytic chemical reaction. Both physical quantities of interest were found to be optimized by the higher value of the magnetic parameter. Then, Shafiq et al. [20] considered the Darcy–Forchheimer flow of nanofluid past a stretched rotating disk with thermal radiation. Based on the RSM and sensitivity analysis, the local Nusselt number was most sensitive towards the solid volume fraction, followed by the radiation parameter and Biot number. Later, Mathew et al. [21] examined the effects of magnetic field and stratification in bioconvective stagnation-point flow over a stretched rotating disk. This study employed the RSM to investigate the relationship between the magnetic field, thermal stratification, the nanoparticle volume fraction of magnetite, and the velocity ratio parameter and the heat transfer rate. The thermal stratification and magnetic field parameters were found to have a negative correlation with the heat transfer rate. Recently, the RSM was utilized by Hussain et al. [22] to optimize the MHD nanofluid flow past a rotating disk with thermal radiation and Joule heating. Meanwhile, Khashi'ie et al. [23] found through the RSM that the magnetic and suction parameters significantly affected the skin friction coefficient in

unsteady hybrid nanofluid flow over a rotating disk with heat generation. In the meantime, the heat transfer rate was affected by the magnetic, suction, and heat generation parameters.

Due to the scarcity of rotating-disk flow studies that combine numerical and statistical investigations, the current research will focus on these approaches to analyze the flow and heat transfer performance in Al_2O_3-Cu/water hybrid nanofluid flow past a shrinking rotating disk. The surface is assumed to be permeable to allow for suction/injection. Partial differential equations and boundary conditions governing this flow problem will be solved numerically using the bvp4c solver in MATLAB. Then, RSM will be executed to analyze the interaction of mass transfer with shrinking parameters and their significance in optimizing the physical quantities of interest. The current study aims to fill the existing literature gap and offer a better understanding of the impacts of mass transfer and shrinking parameters on the considered flow problem.

2. Mathematical Formulation

The working fluid contains alumina (Al_2O_3) and copper (Cu) nanoparticles dispersed in water. This combination is chosen because Cu nanoparticles offer high thermal conductivity, Al_2O_3 nanoparticles exhibit good inertness, and water is widely available. Moreover, an experimental study by Siddiqui et al. [24] demonstrated that an Al_2O_3-Cu/water hybrid nanofluid with a 50:50 mixing ratio resulted in an overall enhanced hydrothermal property with improved thermal conductivity and better stability. Meanwhile, the correlations and values of thermophysical properties for the Al_2O_3-Cu/water hybrid nanofluid are based on Takabi et al. [25] and Oztop and Abu-Nada [26]. At a low-volume concentration of this hybrid nanofluid, the correlations proposed by Takabi et al. [25] were found to be in good agreement with the experiment results presented by Suresh et al. [27]. Following this, a low-volume concentration of Cu and Al_2O_3 nanoparticles is used in the current study (i.e., $\phi_{Al_2O_3} = \phi_{Cu} = 0.02$).

Meanwhile, the flow configuration is described using cylindrical coordinates (r, φ, z) and velocity components (u, v, w), respectively. The schematic representation is depicted in Figure 1.

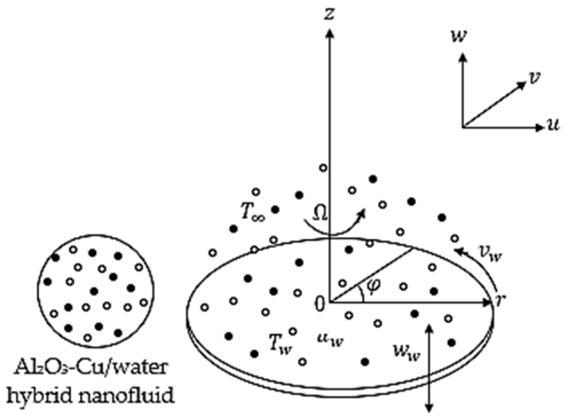

Figure 1. Schematic diagram of the flow problem.

The fluid is assumed to flow in the region $z \geq 0$ over an infinite rotating disk with a uniform shrinking rate a in the radial direction r; angular velocity Ω; mass flux velocity $w_w = \sqrt{\Omega \nu_{bf}} S$ with mass transfer parameter S and kinematic viscosity of base fluid ν_{bf}; and constant temperature T_w. Meanwhile, the surrounding hybrid nanofluid is assumed to have a temperature of T_∞, with $T_w > T_\infty$ for a hot disk. In the current study, the flow is considered to be steady and axisymmetric (i.e., $\partial/\partial\varphi = 0$ for all variables).

Following the stated assumptions, the governing equations and boundary conditions for the laminar, incompressible Newtonian hybrid nanofluid flow are as follows [28,29]:

$$\frac{\partial u}{\partial r} + \frac{u}{r} + \frac{\partial w}{\partial z} = 0, \tag{1}$$

$$u\,\frac{\partial\, u}{\partial\, r} + w\,\frac{\partial\, u}{\partial\, z} - \frac{v^2}{r} = \frac{\mu_{hnf}}{\rho_{hnf}}\left[\frac{1}{r}\frac{\partial u}{\partial r} - \frac{u}{r^2} + \frac{\partial^2 u}{\partial\, r^2} + \frac{\partial^2 u}{\partial\, z^2}\right], \tag{2}$$

$$u\,\frac{\partial\, v}{\partial\, r} + w\,\frac{\partial\, v}{\partial\, z} + \frac{u\,v}{r} = \frac{\mu_{hnf}}{\rho_{hnf}}\left[\frac{1}{r}\frac{\partial v}{\partial r} - \frac{v}{r^2} + \frac{\partial^2 v}{\partial\, r^2} + \frac{\partial^2 v}{\partial\, z^2}\right], \tag{3}$$

$$u\,\frac{\partial\, v}{\partial\, r} + w\,\frac{\partial\, v}{\partial\, z} + \frac{u\,v}{r} = \frac{\mu_{hnf}}{\rho_{hnf}}\left[\frac{1}{r}\frac{\partial v}{\partial r} - \frac{v}{r^2} + \frac{\partial^2 v}{\partial\, r^2} + \frac{\partial^2 v}{\partial\, z^2}\right], \tag{4}$$

$$u\,\frac{\partial\, T}{\partial\, r} + w\,\frac{\partial\, T}{\partial\, z} = \frac{k_{hnf}}{\left(\rho\, C_p\right)_{hnf}}\left[\frac{1}{r}\frac{\partial T}{\partial r} + \frac{\partial^2 T}{\partial\, r^2} + \frac{\partial^2 T}{\partial\, z^2}\right], \tag{5}$$

$$\left.\begin{array}{c} u = u_w = ar, \quad v = v_w = \Omega\, r, \quad w = w_w, \quad T = T_w \quad \text{at} \quad z = 0 \\ u \to 0, \quad v \to 0, \quad T \to T_\infty \quad \text{as} \quad z \to \infty \end{array}\right\}. \tag{6}$$

In these equations, the subscript hnf denotes hybrid nanofluid, μ is the dynamic viscosity, ρ is the density, k is the thermal conductivity, C_p is the specific heat, T is the temperature, and p is the pressure. Then, these partial differential equations are subjected to the following Von Kármán's transformations [2]:

$$\left.\begin{array}{c} u = \Omega\, r f(\eta), \quad v = \Omega\, r g(\eta), \quad w = \sqrt{\Omega\, \nu_{bf}}\, h(\eta), \quad \theta(\eta) = \frac{T - T_\infty}{T_w - T_\infty} \\ p - p_\infty = 2\,\mu_{bf}\,\Omega\, P(\eta), \quad \eta = z\sqrt{\frac{\Omega}{\nu_{bf}}} \end{array}\right\} \tag{7}$$

to form the following non-linear ordinary differential equations and boundary conditions:

$$2\, f + h' = 0, \tag{8}$$

$$\frac{\mu_{hnf}/\mu_{bf}}{\rho_{hnf}/\rho_{bf}} f'' - h f' - f^2 + g^2 = 0, \tag{9}$$

$$\frac{\mu_{hnf}/\mu_{bf}}{\rho_{hnf}/\rho_{bf}} g'' - h\, g' - 2 f g = 0, \tag{10}$$

$$\frac{k_{hnf}/k_{bf}}{\left(\rho\, C_p\right)_{hnf}/\left(\rho\, C_p\right)_{bf}} \theta'' - Prh\, \theta' = 0, \tag{11}$$

$$\left.\begin{array}{c} g(0) = 1, \quad f(0) = \lambda, \quad h(0) = S, \quad \theta(0) = 1 \\ g(\eta) \to 0, \quad f(\eta) \to 0, \quad \theta(\eta) \to 0 \quad as \quad \eta \to \infty \end{array}\right\}, \tag{12}$$

where '$\prime$' denotes differentiation with respect to η; bf refers to the base fluid; f, g, and h are the radial, tangential, and axial velocities; $\lambda = a/\Omega$ is the shrinking parameter; S is the mass transfer parameter with $S < 0$ for injection and $S > 0$ for suction; and $Pr = \left(\mu\, C_p\right)_{bf}/k_{bf}$ is the Prandtl number. According to Turkyilmazoglu [28], the fluid pressure can be determined by integrating Equation (4), and the resulting pressure equation is decoupled from the flow field. Since the interest of the current study is to analyze the flow and thermal fields of the hybrid nanofluid, the pressure function can be neglected.

Then, the physical quantities of interest are the skin friction coefficient (C_f) and Nusselt number (Nu_r) [28]:

$$C_f = \frac{\mu_{hnf}\sqrt{\left[\left(\frac{\partial u}{\partial z} + \frac{\partial w}{\partial \varphi}\right)_{z=0}\right]^2 + \left[\left(\frac{\partial v}{\partial z} + \frac{1}{r}\frac{\partial w}{\partial \varphi}\right)_{z=0}\right]^2}}{\rho_{bf}(\Omega r)^2},$$

$$Nu_r = \frac{r\,k_{nf}}{k_{bf}(T_w - T_\infty)}\left(-\frac{\partial T}{\partial z}\right)_{z=0},$$

which result in the following:

$$Re_r^{1/2}C_f = \frac{\mu_{hnf}}{\mu_{bf}}\sqrt{[f'(0)]^2 + [g'(0)]^2}, \quad Re_r^{-1/2}Nu_r = -\frac{k_{hnf}}{k_{bf}}\theta'(0), \tag{13}$$

where $Re_r^{1/2}C_f$ is the local skin friction coefficient; $Re_r^{-1/2}Nu_r$ is the local Nusselt number; and $Re_r = \frac{\Omega r^2}{\nu_{bf}}$ is the local Reynolds number. Here, an increase in the angular velocity can raise the local Reynolds number.

3. Response Surface Methodology (RSM)

Box and Wilson [30] introduced an experimental design-based approach, incorporating statistical and mathematical techniques, called the response surface methodology (RSM). The RSM can be used to model, analyze, and optimize a system containing dependent (response) and independent parameters. The relationship between the response and independent parameters can be described as follows [31]:

$$\text{Response} = F(X_1, X_2, X_3, \ldots, X_N) \pm E, \tag{14}$$

where F is the unknown function of response with $X_1, X_2, X_3, \ldots, X_N$ as independent parameters; and E is the random experimental error assumed to have a zero mean. Meanwhile, the general quadratic model is

$$\text{Response} = c_0 + \sum_{i=1}^{N} c_i x_i + \sum_{i=1}^{N} c_{ii} x_i^2 + \sum_{i=1}^{N-1}\sum_{j=i+1}^{N} c_{ij} x_i x_j, \tag{15}$$

with c_0, c_i, c_{ii}, and c_{ij} representing the intercept, linear, quadratic, and bilinear two-factor terms, respectively.

The current study utilizes the RSM and face-centered central composite design to investigate the significance of the mass transfer and shrinking parameters on the local skin friction coefficient and Nusselt number, as well as the optimal settings of these parameters to minimize and maximize the responses. Therefore, the mass transfer and shrinking parameters are denoted as the independent parameters, and the local skin friction coefficient and Nusselt number are the responses. The independent parameters are labeled as A and B and are assigned with actual and coded values, as shown in Table 1. The ranges for the actual values are taken based on the numerical investigation conducted in the current study.

Table 1. The actual and coded values of the independent parameters.

Independent Parameter	Symbol	Level		
		Low (−1)	Medium (0)	High (1)
λ	A	−1.0	−0.9	−0.8
S	B	−0.6	−0.1	0.4

The central composite design is the most commonly used response surface design to determine the coefficients of the quadratic model. According to Bhattacharya [32], the

central composite design has the benefit of estimating the non-linear relationship between the independent parameters and the response, as well as the ability to provide maximum information with minimal experimental data, and fewer experiments are needed to predict the quadratic term in a quadratic model. The central composite design is comprised of several types, including the face-centered type. The face-centered central composite design requires three levels of each factor or independent parameter (i.e., -1, 0, 1) with $2^N + 2N + C$ experiments. Here, N is the number of independent parameters; 2^N denotes the factorial points; $2N$ denotes the axial points; and C denotes the center points. As stated by Sahoo and Barman [33], the center points may vary from three to six. In this current study, with $N = 2$ and $C = 5$, a total of 13 runs are carried out. The respective responses, calculated using MATLAB for each run, are then tabulated in Table 2. Meanwhile, Figure 2 presents the flowchart of the numerical and statistical procedures involved in the current study.

Table 2. Experimental design and response values.

Runs	Coded Values		Actual Values		Responses	
	A	**B**	λ	S	$Re_r^{1/2}Cf$ **(Response 1)**	$Re_r^{-1/2}Nu_r$ **(Response 2)**
1	−1	−1	−1.0	−0.6	1.803245471	0.232133118
2	1	−1	−0.8	−0.6	1.529299905	0.975650061
3	−1	1	−1.0	0.4	1.475361873	0.000000014
4	1	1	−0.8	0.4	1.229514429	0.000001138
5	−1	0	−1.0	−0.1	1.642240690	0.000228587
6	1	0	−0.8	−0.1	1.380007580	0.004928016
7	0	−1	−0.9	−0.6	1.659170147	0.525530320
8	0	1	−0.9	0.4	1.346068736	0.000000126
9	0	0	−0.9	−0.1	1.504436107	0.001106468
10	0	0	−0.9	−0.1	1.504436107	0.001106468
11	0	0	−0.9	−0.1	1.504436107	0.001106468
12	0	0	−0.9	−0.1	1.504436107	0.001106468
13	0	0	−0.9	−0.1	1.504436107	0.001106468

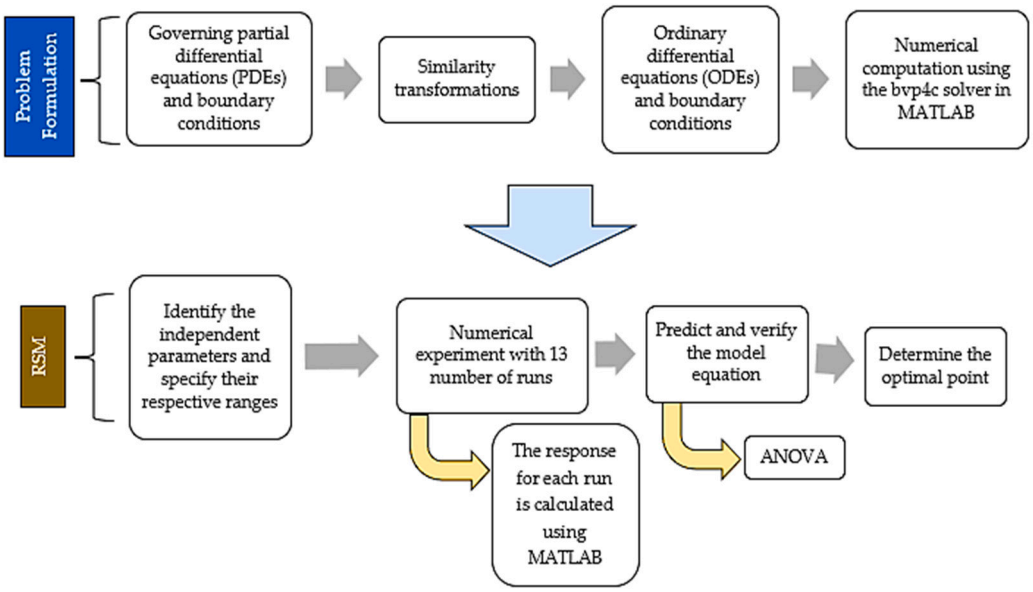

Figure 2. Flowchart of the numerical and statistical procedures.

4. Results and Discussion

The boundary value problem (8)–(12) is numerically solved using the bvp4c solver in MATLAB, and the algorithm is presented in Supplementary Materials. A comparison of

results is made to validate the correctness of the mathematical approach employed in this current study. For $\phi_{hnf} = 0$, the boundary value problem reduces into a classical viscous fluid flow problem, and the numerical results can be compared with those computed by Rashidi et al. [34] and Turkyilmazoglu [28]. These previous studies utilized the shooting and spectral Chebyshev collocation methods, respectively. Despite the difference in computation techniques, the results generated by the bvp4c solver are in close agreement with the previous studies (see Table 3). Furthermore, by assuming the finite value of the free stream boundary condition (i.e., $\eta \to \infty$) to be $\eta_{\max} = 10$, all profiles acquired in this investigation approach the free stream boundary conditions (12) asymptotically. Therefore, it enhances confidence in the reliability of the numerical findings.

Table 3. Comparison of results for $\phi_{Al_2O_3} = \phi_{Cu} = S = \lambda = 0$ and $Pr = 6.2$.

	Rashidi et al. [34]	**Turkyilmazoglu [28]**	**Present Study**
$f'(0)$	0.510186	0.51023262	0.510232394
$-g'(0)$	0.61589	0.61592201	0.615921866
$-\theta'(0)$	-	0.93387794	0.933877577

The effects of shrinking and mass transfer parameters on the velocity and temperature profiles are presented in Figure 3. The radial, tangential, and axial velocities are denoted by $f(\eta)$, $g(\eta)$, and $h(\eta)$, respectively. As observed in Figure 3a, the radial velocity profile of the hybrid nanofluid decreases with the augmentation of the mass transfer parameter and the magnitude of the shrinking parameter. However, the opposite behavior is observed at some distance from the disk. As the disk is assumed to have a no-slip condition and to shrink in the radial direction, the radial velocity of the hybrid nanofluid near the disk decreases as the magnitude of the shrinking parameter increases. The shrinking effects towards the fluid velocity are shown to be diminished at some distance away from the disk (see Figure 3a). Meanwhile, the shrinking of the disk does not affect the tangential and axial velocities of the hybrid nanofluid. The tangential velocity of the hybrid nanofluid continues to increase throughout the boundary layer when the mass transfer parameter and magnitude of the shrinking parameter increase (see Figure 3b). Figure 3c demonstrates that the axial velocity profile near the disk rises with both the mass transfer parameter and the magnitude of the shrinking parameter. As the mass transfer occurs in the axial direction, the fluid velocity increases with the mass transfer parameter. Meanwhile, the radial velocity near the disk, shown in Figure 3a, decreases due to fluid removal from the boundary by suction ($S > 0$). The increment in the mass transfer parameter and magnitude of the shrinking parameter then enhances the temperature profile, as shown in Figure 3d.

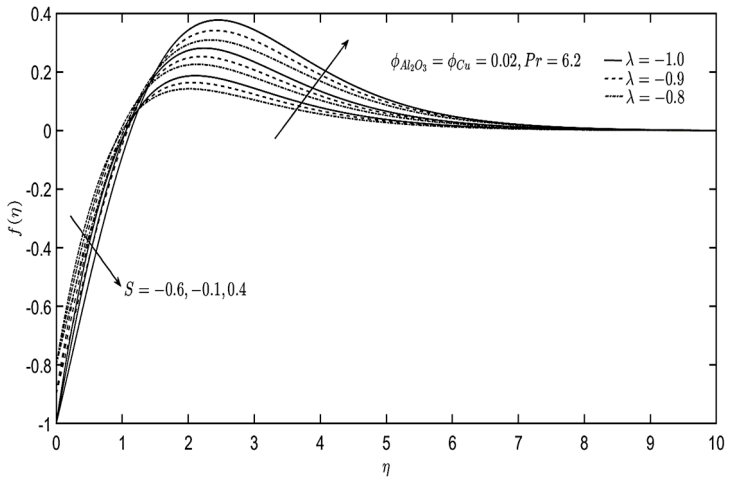

(**a**)

Figure 3. *Cont.*

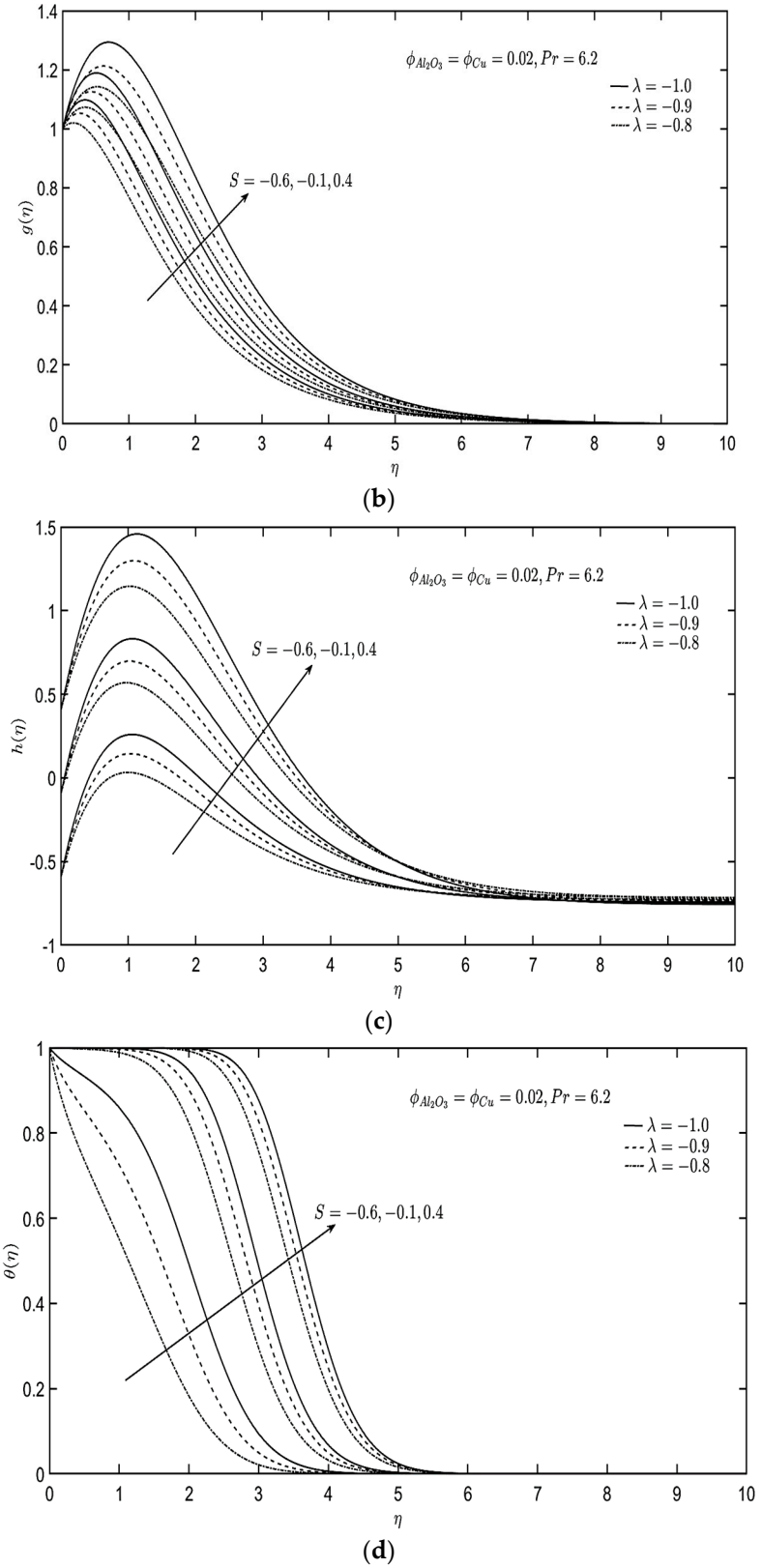

Figure 3. The profiles of (**a**) radial velocity, (**b**) tangential velocity, (**c**) axial velocity, and (**d**) temperature with various values of λ and S.

Next, the effects of shrinking and mass transfer parameters on the local skin friction coefficient and Nusselt number are illustrated in Figure 4. The enhancement of the mass transfer parameter is found to reduce the local skin friction coefficient and Nusselt number

in Figure 4a,b, respectively. Meanwhile, the increment in the magnitude of the shrinking parameter raises the local skin friction coefficient, as shown in Figure 4a. Thus, the wall shear stress rises with the increase in the magnitude of the shrinking parameter. In contrast, the local Nusselt number diminishes as $|\lambda|$ increases. The observed behavior may be due to the reduction of the surface area available for heat transfer. Hence, it causes the heat transfer rate between the disk and hybrid nanofluid to decrease. Moreover, it can be noted that the values of the local skin friction coefficient and Nusselt number for the injection case ($S < 0$) are higher than the suction case ($S > 0$).

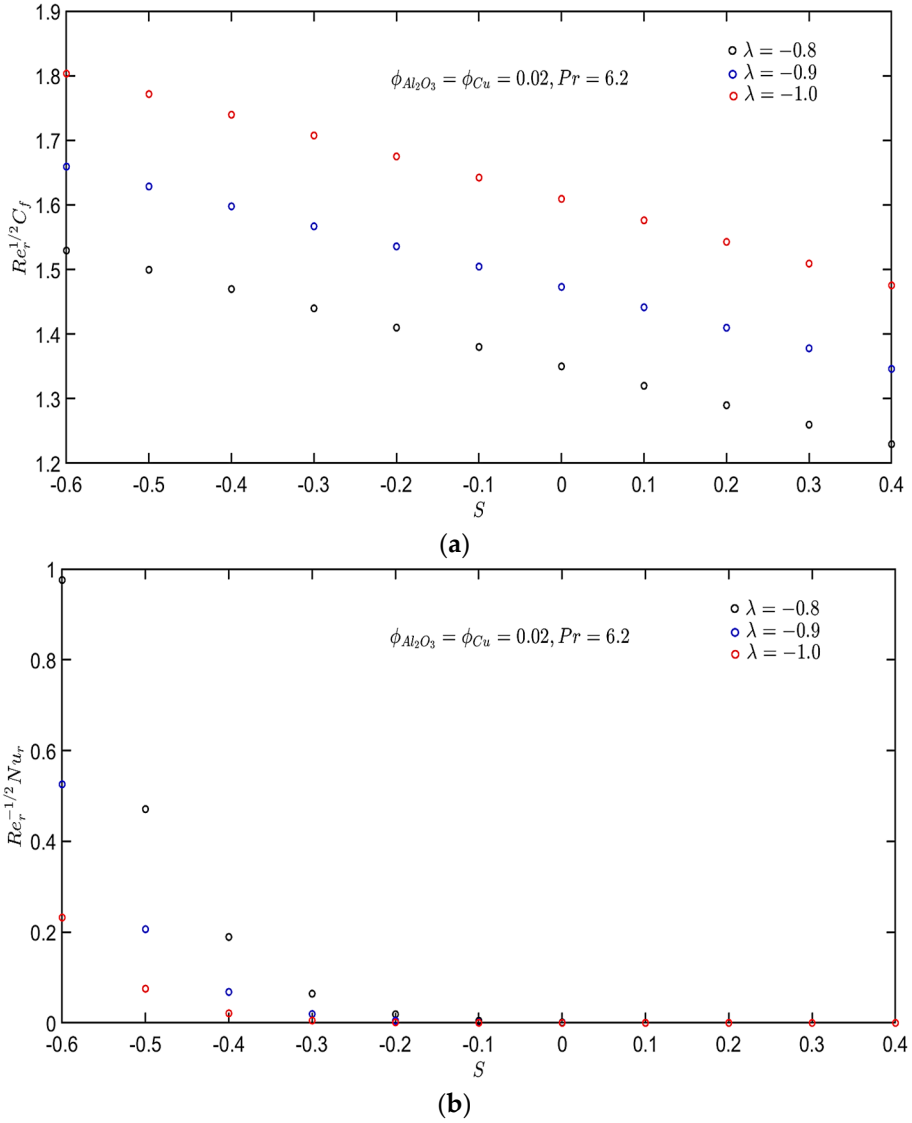

Figure 4. The profiles of (**a**) local skin friction coefficient and (**b**) local Nusselt number with various values of λ and S.

Meanwhile, the interacting impacts of the shrinking and mass transfer parameters on the physical quantities of interest are analyzed using the RSM in Minitab. The correlations between the independent parameters and the responses are given by the following:

$$\text{Response } 1 = c_0 + c_1\text{A} + c_2\text{B} + c_{11}\text{AA} + c_{22}\text{BB} + c_{12}\text{AB}, \tag{16}$$

$$\text{Response } 2 = c_0 + c_1\text{A} + c_2\text{B} + c_{11}\text{AA} + c_{22}\text{BB} + c_{12}\text{AB}. \tag{17}$$

The significance of each term in Equations (16) and (17) are identified through the analysis of variance (ANOVA). The results are presented in Tables 4 and 5.

Table 4. Analysis of variance for Response 1.

Source	DF	Adj SS	Adj MS	F-Value	*p*-Value
Model	5	0.249759313	0.049951863	174774.611709837	0.000000000
Linear	2	0.249435660	0.124717830	436370.320105496	0.000000000
A	1	0.101927475	0.101927475	356630.043436460	0.000000000
B	1	0.147508184	0.147508184	516110.596774533	0.000000000
Square	2	0.000126277	0.000063139	220.913397825	0.000000474
AA	1	0.000124396	0.000124396	435.243856915	0.000000146
BB	1	0.000008884	0.000008884	31.084684334	0.000837291
2-Way Interaction	1	0.000197376	0.000197376	690.591542539	0.000000030
AB	1	0.000197376	0.000197376	690.591542539	0.000000030
Error	7	0.000002001	0.000000286		
Lack-of-Fit	3	0.000002001	0.000000667	*	*
Pure Error	4	0.000000000	0.000000000		
Total	12	0.249761314			

The symbol * denotes the value is too small.

Table 5. Analysis of variance for Response 2.

Source	DF	Adj SS	Adj MS	F-Value	*p*-Value
Model	5	1.000087703	0.200017541	29.206710770	0.000150454
Linear	2	0.594033446	0.297016723	43.370603881	0.000113785
A	1	0.093304904	0.093304904	13.624451749	0.007745032
B	1	0.500728543	0.500728543	73.116756012	0.000059439
Square	2	0.267850314	0.133925157	19.555851501	0.001363026
AA	1	0.001069278	0.001069278	0.156136818	0.704502971
BB	1	0.216321666	0.216321666	31.587451304	0.000798846
2-Way Interaction	1	0.138203943	0.138203943	20.180643085	0.002824322
AB	1	0.138203943	0.138203943	20.180643085	0.002824322
Error	7	0.047938393	0.006848342		
Lack-of-Fit	3	0.047938393	0.015979464	*	*
Pure Error	4	0.000000000	0.000000000		
Total	12	1.048026096			

The symbol * denotes the value is too small.

The symbol * denotes the value is too small.

According to Alhadri et al. [35], a term is statistically significant if its p-value is less than 0.05. Based on Tables 4 and 5, all terms are significant for correlation (16), while the term AA can be removed from correlation (17) as its p-value is greater than 0.05. After eliminating the insignificant term, a second ANOVA is carried out for Response 2. Then, the following new correlations, containing only the significant terms, are obtained:

$$\text{Response 1} = 1.50443 - 0.130338\text{A} - 0.156795\text{B} + 0.006711\text{AA} - 0.001794\text{BB} + 0.007025\text{AB}, \quad (18)$$

$$\text{Response 2} = 0.0015 + 0.1247\text{A} - 0.2889\text{B} + 0.2874\text{BB} - 0.1859\text{AB}. \quad (19)$$

Based on Equations (18) and (19), the term B is seen to have a negative correlation with Response 1 and Response 2. Hence, the increment in the mass transfer parameter has an unfavorable impact on the local skin friction coefficient and Nusselt number. These findings agree with the results obtained in Figure 4.

Then, the interactive impacts between the shrinking and mass transfer parameters can be analyzed through the surface and contour plots displayed in Figures 5 and 6. Based on Figure 5, the increase in A and B reduces Response 1. The higher and medium levels of shrinking parameter (A) and mass transfer parameter (B) are observed to produce low values of $Re_r^{1/2}C_f$ (Response 1). The maximum $Re_r^{1/2}C_f$ (Response 1) occurs at low levels

of these independent parameters. Meanwhile, Figure 6 shows that lower levels of the mass transfer parameter (B) and higher levels of the shrinking parameter (A) produce high values of $Re_r^{-1/2}Nu_r$ (Response 2). However, at the moderate level of mass transfer parameter (B), the increment in the shrinking parameter (A) has no significant effect on $Re_r^{-1/2}Nu_r$ (Response 2).

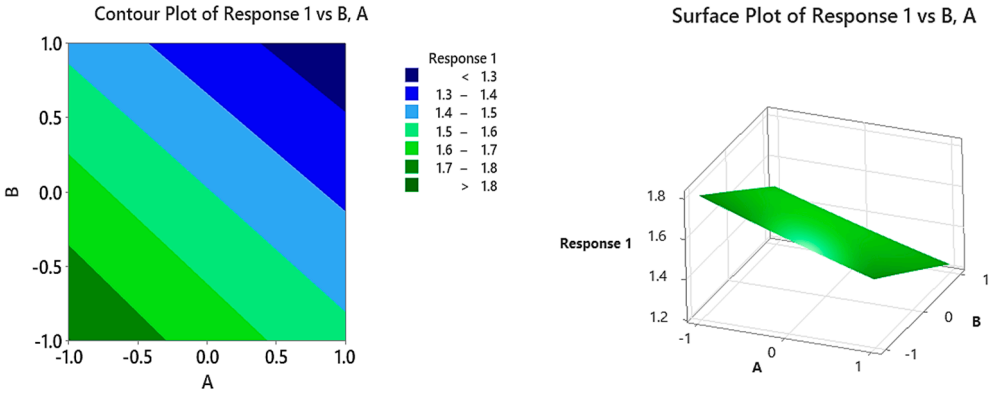

Figure 5. Contour and surface plots for Response 1.

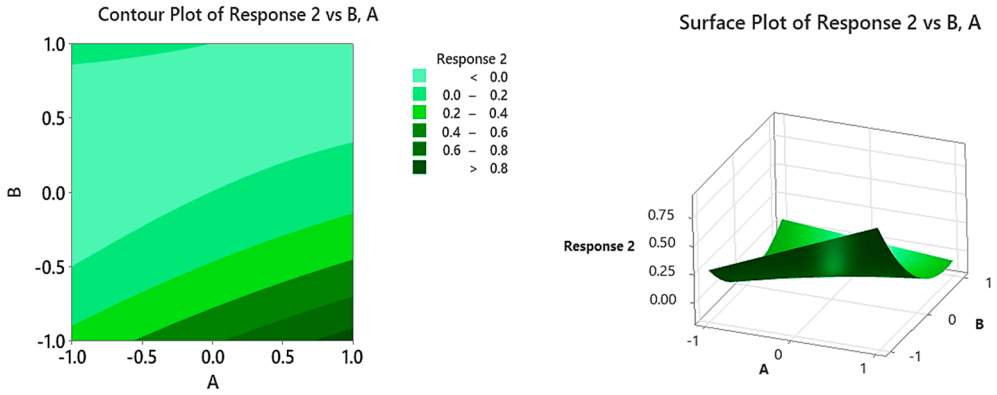

Figure 6. Contour and surface plots for Response 2.

Next, optimization is conducted to minimize and maximize the local skin friction coefficient and Nusselt number, respectively. The local skin friction coefficient is related to the wall shear stress. A low skin friction coefficient is sought to reduce energy consumption in most applications. Meanwhile, a high heat transfer rate, represented by the local Nusselt number, is desired for better heat transfer performance in cooling or heating processes. The composite desirability assesses how the configurations of the independent parameters optimize a given set of responses. The desirability is measured on a scale from zero to one. A value of zero signifies that one or more responses exceed their permissible limits, whereas a value of one represents the optimal scenario. Therefore, in the present investigation, the optimization can be observed by examining the composite desirability.

Table 6 presents the optimization result for the local skin friction coefficient and Nusselt number. The minimum local skin friction coefficient (Response 1) and maximum local Nusselt number (Response 2) can be achieved by setting the shrinking parameter (A) and mass transfer parameter (B) at high and low levels, respectively. With a desirability of 66% at $\lambda = -0.8$ and $S = -0.6$, the local skin friction coefficient is minimized at 1.528780016, while the local Nusselt number is maximized at 0.888353037. Hence, the lowest magnitude of the shrinking parameter and lowest mass transfer parameter optimized the physical quantities of interest in the current flow problem. Different behavior may be observed for other controlling parameters and flow conditions ranges.

Table 6. Optimization of responses.

Solution	A	B	Response 2 Fit	Response 1 Fit	Composite Desirability
1	1	−1	0.888353037	1.528780016	0.659986551

5. Conclusions

The current study analyzes the rotating-disk flow of a hybrid nanofluid. The disk is considered to shrink in the radial direction and is permeable to allow for suction/injection. The local skin friction coefficient and Nusselt number for this flow problem are optimized using the RSM. First, the governing equations for the flow problem, consisting of differential equations and boundary conditions, are presented and solved using the bvp4c solver in MATLAB. Then, the Minitab 21 software is utilized to perform the RSM. The results are outlined as follows:

1. As the mass transfer parameter and the magnitude of the shrinking parameter ($|\lambda|$) increase, the radial velocity profile of the hybrid nanofluid near the disk decreases.
2. The increment in the mass transfer parameter and the magnitude of the shrinking parameter improves the profiles of tangential velocity, axial velocity, and temperature.
3. The local skin friction coefficient and Nusselt number diminish with the increase in the mass transfer parameter. The injection case demonstrates higher values of these physical quantities of interest than the suction case.
4. The increment in the magnitude of the shrinking parameter enhances the local skin friction coefficient and reduces the local Nusselt number.
5. Based on the RSM, low values of $Re_r^{1/2}C_f$ are produced at higher and medium levels of shrinking parameter (λ) and mass transfer parameter. Meanwhile, the highest value of $Re_r^{1/2}C_f$ is observed at low levels of these independent parameters.
6. High values of $Re_r^{-1/2}Nu_r$ occur at lower levels of the mass transfer parameter and higher levels of the shrinking parameter.
   The local Nusselt number is not significantly impacted by the increase in the shrinking parameter at the moderate level of the mass transfer parameter.
7. With a desirability of 66%, the local skin friction coefficient is minimized at 1.528780016, while the local Nusselt number is maximized at 0.888353037 when $\lambda = -0.8$ and $S = -0.6$.

The current study can be extended to other types of hybrid nanofluids, such as non-Newtonian hybrid nanofluids, carbon nanotubes hybrid nanofluids, and ternary hybrid nanofluids. In addition, the complex non-linear interaction of various controlling parameters in this flow problem can be further analyzed using a sophisticated machine learning technique known as the artificial neural network (ANN).

Supplementary Materials: The following supporting information can be downloaded at: https://www.mdpi.com/article/10.3390/computation12070141/s1.

Author Contributions: Conceptualization, I.P.; methodology, I.P. and R.I.Y.; validation, I.P. and N.M.A.; formal analysis, R.I.Y.; writing—original draft preparation, R.I.Y. and I.P.; writing—review and editing, N.M.A. and I.P.; supervision, N.M.A., F.M.A. and S.S.P.M.I.; funding acquisition, N.M.A. All authors have read and agreed to the published version of the manuscript.

Funding: This research was funded by Universiti Putra Malaysia, grant number GP-GPB 9711400.

Data Availability Statement: The original contributions presented in the study are included in the article/Supplementary Materials, further inquiries can be directed to the corresponding author/s.

Conflicts of Interest: The authors declare no conflicts of interest. The funders had no role in the design of the study; in the collection, analyses, or interpretation of data; in the writing of the manuscript; or in the decision to publish the results.

References

1. Gamachu, D.; Ibrahim, W. Mixed Convection Flow of Viscoelastic Ag-Al_2O_3/Water Hybrid Nanofluid Past a Rotating Disk. *Phys. Scr.* **2021**, *96*, 125205. [CrossRef]
2. Kármán, T.V. Über Laminare Und Turbulente Reibung. *ZAMM J. Appl. Math. Mech. Z. Angew. Math. Mech.* **1921**, *1*, 233–252. [CrossRef]
3. Ayano, M.S.; Otegbeye, O.; Mathunjwa, J.S. Numerical Simulation Of Nanofluid Flow Due To A Stretchable Rotating Disk. *Theor. Appl. Mech.* **2023**, *50*, 55–72. [CrossRef]
4. Sharma, K.; Vijay, N.; Bhardwaj, D.; Jindal, R. Flow of Water Conveying Fe_3O_4 and Mn–$ZnFe_2O_4$ Nanoparticles over a Rotating Disk: Significance of Thermophoresis and Brownian Motion. *J. Magn. Magn. Mater.* **2023**, *574*, 170710. [CrossRef]
5. Puneeth, V.; Aly, E.H.; Pop, I. Nanofluid Flowing over a Rotating Disk That Is Stretching and Permeable: An Unsteady Model. *Int. J. Mod. Phys. B* **2023**, *37*, 23502491. [CrossRef]
6. Rashid, A.; Dawar, A.; Ayaz, M.; Islam, S.; Galal, A.M.; Gul, H. Homotopic Solution of the Chemically Reactive Magnetohydrodynamic Flow of a Hybrid Nanofluid over a Rotating Disk with Brownian Motion and Thermophoresis Effects. *ZAMM Z. Angew. Math. Mech.* **2023**, *103*, e202200262. [CrossRef]
7. Alkuhayli, N.A.M. Heat Transfer Analysis of a Hybrid Nanofluid Flow on a Rotating Disk Considering Thermal Radiation Effects. *Case Stud. Therm. Eng.* **2023**, *49*, 103131. [CrossRef]
8. Kumar, P.; Poonia, H.; Areekara, S.; Sabu, A.S.; Mathew, A.; Ali, L. Significance of Irregular Heat Source and Arrhenius Energy on Electro-Magnetohydrodynamic Hybrid Nanofluid Flow over a Rotating Stretchable Disk with Nonlinear Radiation. *Numer. Heat. Transf. A Appl.* **2024**, *85*, 1866–1888. [CrossRef]
9. Kulkarni, M. Mixed Convective Magnetized GO-MoS_2/H_2O Hybrid Nanofluid Flow about a Permeable Rotating Disk. *Asia Pac. J. Chem. Eng.* **2023**, *18*, e2923. [CrossRef]
10. Lone, S.A.; Anwar, S.; Raizah, Z.; Almusawa, M.Y.; Saeed, A. A Theoretical Investigation of the MHD Water-Based Hybrid Nanofluid Flow over a Convectively Heated Rotating Disk Surface with Velocity Slips and Zero Mass Flux Conditions. *Eur. Phys. J. Plus* **2023**, *138*, 1–14. [CrossRef]
11. Khashi'ie, N.S.; Waini, I.; Zainal, N.A.; Hamzah, K.; Arifin, N.M.; Pop, I. Multiple Solutions and Stability Analysis of Magnetic Hybrid Nanofluid Flow Over a Rotating Disk with Heat Generation. *J. Adv. Res. Fluid. Mech. Therm. Sci.* **2023**, *102*, 59–72. [CrossRef]
12. Vijay, N.; Sharma, K. Magnetohydrodynamic Hybrid Nanofluid Flow over a Decelerating Rotating Disk with Soret and Dufour Effects. *Multidiscip. Model. Mater. Struct.* **2023**, *19*, 253–276. [CrossRef]
13. Abu Bakar, S.; Pop, I.; Md Arifin, N. Unsteady Flow of Hybrid Nanofluid over a Permeable Shrinking Inclined Rotating Disk with Radiation and Velocity Slip Effects. *Neural Comput. Appl.* **2024**, *36*, 11525–11544. [CrossRef]
14. Ali, F.; Zaib, A.; Khan, M.I.; Alzahrani, F.; Eldin, S.M. Irreversibility Analysis in Stagnation Point Flow of Tri-Hybrid Nanofluid over a Rotating Disk; Application of Kinetic Energy. *J. Indian. Chem. Soc.* **2023**, *100*, 100873. [CrossRef]
15. Singh, S.P.; Kumar, M.; Yaseen, M.; Rawat, S.K. Ternary Hybrid Nanofluid ($TiO_2-SiO_2-MoS_2$/Kerosene Oil) Flow over a Rotating Disk with Quadratic Thermal Radiation and Cattaneo-Christov Model. *J. Cent. S. Univ.* **2023**, *30*, 1262–1278. [CrossRef]
16. Patgiri, B.; Paul, A. Inspection of Viscoelastic Ag+Cu+Fe_3O_4+Al_2O_3/Kerosene Oil Tetra-Hybrid Nanofluid Flow across a Stretchable Rotating Disk with Exponentially Varying Viscosity. *J. Taibah Univ. Sci.* **2024**, *18*, 2336327.
17. Ali, I.; Gul, T.; Khan, A. Unsteady Hydromagnetic Flow over an Inclined Rotating Disk through Neural Networking Approach. *Mathematics* **2023**, *11*, 1893. [CrossRef]
18. Varun Kumar, R.S.; Kumar, R.N.; Ben Ahmed, S.; Madhu, J.; Verma, A.; Punith Gowda, R.J. Unsteady Flow of a Ternary Nanofluid over a Slow-Rotating Disk Subject to Uniform Suction and Backpropagated Neural Network. *Numer. Heat Transf. Part B Fundam.* **2023**, 1–21. [CrossRef]
19. Mehmood, T.; Ramzan, M.; Howari, F.; Kadry, S.; Chu, Y.M. Application of Response Surface Methodology on the Nanofluid Flow over a Rotating Disk with Autocatalytic Chemical Reaction and Entropy Generation Optimization. *Sci. Rep.* **2021**, *11*, 4021. [CrossRef]
20. Shafiq, A.; Sindhu, T.N.; Al-Mdallal, Q.M. A Sensitivity Study on Carbon Nanotubes Significance in Darcy–Forchheimer Flow towards a Rotating Disk by Response Surface Methodology. *Sci. Rep.* **2021**, *11*, 8812. [CrossRef]
21. Mathew, A.; Areekara, S.; Sabu, A.S. Significance of Magnetic Field and Stratification Effects on the Bioconvective Stagnation-Point Flow of Ferro-Nanofluid over a Rotating Stretchable Disk: Four-Factor Response Surface Methodology. *J. Indian Chem. Soc.* **2022**, *99*, 100615. [CrossRef]
22. Hussain, S.; Ali, A.; Rasheed, K.; Pasha, A.A.; Algarni, S.; Alqahtani, T.; Irshad, K. Application of Response Surface Methodology to Optimize MHD Nanofluid Flow over a Rotating Disk with Thermal Radiation and Joule Heating. *Case Stud. Therm. Eng.* **2023**, *52*, 103715. [CrossRef]
23. Khashi'ie, N.S.; Waini, I.; Hamzah, K.B.; Mukhtar, M.F.; Kasim, A.R.M.; Arifin, N.M.; Pop, I. Numerical Solution and Statistical Analysis of the Unsteady Hybrid Ferrofluid Flow with Heat Generation Subject to a Rotating Disk. *ZAMM J. Appl. Math. Mech. Z. Angew. Math. Mech.* **2023**, *103*, e202200384. [CrossRef]
24. Siddiqui, F.R.; Tso, C.Y.; Chan, K.C.; Fu, S.C.; Chao, C.Y.H. On Trade-off for Dispersion Stability and Thermal Transport of Cu-Al_2O_3 Hybrid Nanofluid for Various Mixing Ratios. *Int. J. Heat Mass Transf.* **2019**, *132*, 1200–1216. [CrossRef]

25. Takabi, B.; Gheitaghy, A.M.; Tazraei, P. Hybrid Water-Based Suspension of Al_2O_3 and Cu Nanoparticles on Laminar Convection Effectiveness. *J. Thermophys. Heat Trans.* **2016**, *30*, 523–532. [CrossRef]
26. Oztop, H.F.; Abu-Nada, E. Numerical Study of Natural Convection in Partially Heated Rectangular Enclosures Filled with Nanofluids. *Int. J. Heat Fluid Flow* **2008**, *29*, 1326–1336. [CrossRef]
27. Suresh, S.; Venkitaraj, K.P.; Selvakumar, P.; Chandrasekar, M. Synthesis of Al_2O_3-Cu/Water Hybrid Nanofluids Using Two Step Method and Its Thermo Physical Properties. *Colloids Surf. A Physicochem. Eng. Asp.* **2011**, *388*, 41–48. [CrossRef]
28. Turkyilmazoglu, M. Nanofluid Flow and Heat Transfer Due to a Rotating Disk. *Comput. Fluids* **2014**, *94*, 139–146. [CrossRef]
29. Yin, C.; Zheng, L.; Zhang, C.; Zhang, X. Flow and Heat Transfer of Nanofluids over a Rotating Disk with Uniform Stretching Rate in the Radial Direction. *Propuls. Power Res.* **2017**, *6*, 25–30. [CrossRef]
30. Box, G.E.P.; Wilson, K.B. On the Experimental Attainment of Optimum Conditions. *J. R. Stat. Soc. Ser. B (Methodol.)* **1951**, *13*, 1–38. [CrossRef]
31. Mahanthesh, B.; Thriveni, K.; Rana, P.; Muhammad, T. Radiative Heat Transfer of Nanomaterial on a Convectively Heated Circular Tube with Activation Energy and Nanoparticle Aggregation Kinematic Effects. *Int. Commun. Heat Mass Transf.* **2021**, *127*, 105568. [CrossRef]
32. Bhattacharya, S. Central Composite Design for Response Surface Methodology and Its Application in Pharmacy. In *Response Surface Methodology in Engineering Science*; IntechOpen: London, UK, 2021.
33. Sahoo, P.; Barman, T.K. ANN Modelling of Fractal Dimension in Machining. In *Mechatronics and Manufacturing Engineering*; Woodhead Publishing: Cambridge, UK, 2012.
34. Rashidi, M.M.; Abelman, S.; Mehr, N.F. Entropy Generation in Steady MHD Flow Due to a Rotating Porous Disk in a Nanofluid. *Int. J. Heat Mass Transf.* **2013**, *62*, 515–525. [CrossRef]
35. Alhadri, M.; Raza, J.; Yashkun, U.; Lund, L.A.; Maatki, C.; Khan, S.U.; Kolsi, L. Response Surface Methodology (RSM) and Artificial Neural Network (ANN) Simulations for Thermal Flow Hybrid Nanofluid Flow with Darcy-Forchheimer Effects. *J. Indian Chem. Soc.* **2022**, *99*, 100607. [CrossRef]